Nanoscale Horizons

ROYAL SOCIETY OF CHEMISTRY

COMMUNICATION

View Article Online
View Journal | View Issue

Check for updates

Cite this: *Nanoscale Horiz.*, 2025, **10**, 2465

Received 1st April 2025,
Accepted 25th June 2025

DOI: 10.1039/d5nh00198f

rsc.li/nanoscale-horizons

Open Access Article. Published on 01 2025. Downloaded on 2026/5/15 03:53:08.
This article is licensed under a Creative Commons Attribution 3.0 Unported Licence.

Interplay between charge transfer and magnetic proximity effects in $WSe_2/CrCl_3$ heterostructures†

Łucja Kipczak, ‡*[a] Zhaolong Chen,‡[g] Magdalena Grzeszczyk,[b] Sergey Grebenchuk,[bc] Pengru Huang,[bd] Kristina Vaklinova,[b] Kenji Watanabe,[e] Takashi Taniguchi,[f] Adam Babiński,[a] Maciej Koperski *[bc] and Maciej R. Molas *[a]

Ferromagnetism in van der Waals systems with diverse spin arrangements opened a pathway to use proximity magnetic fields to activate the properties of materials that would otherwise require external stimuli. Herein, we demonstrate this concept by creating heterostructures comprising a bulk $CrCl_3$ antiferromagnet with in-plane easy-axis magnetization and a monolayer (ML) WSe_2 semiconductor. Photoluminescence and magnetic force microscopy techniques were performed to reveal the interaction between the relevant layers in the $WSe_2/CrCl_3$ heterostructures (HSs). The quenching of the WSe_2 emission is apparent in the $WSe_2/CrCl_3$ HSs due to an efficient charge transfer process enabled by the relative band alignment within the structures. Moreover, we demonstrate that at specific spatial locations in the structures, the magnetic proximity effect between the WSe_2 ML and the $CrCl_3$ bulk activates dark exciton emission within the WSe_2 ML. The dark exciton emission in the WSe_2 ML survives to a higher temperature than the intraplane Curie temperature (T_C) of the $CrCl_3$ because of its elevated T_C in the strained regions of the $CrCl_3$ layer. Our findings are relevant to the development of spintronics and valleytronics with long-lived dark states on technological timescales, as well as to sensing applications of local magnetic fields realized simultaneously in multiple dimensions.

New concepts

Dark excitons in monolayer semiconductors are technologically relevant spin states due to their long radiative lifetimes in MHz ranges and extended spin coherence. So far, the emission of the dark states has been achieved exclusively *via* the application of external in-plane magnetic fields driven by spin mixing occurring between K^+ and K^- valleys. In this work, we realized a new concept of activating the dark excitons intrinsically in heterostructures comprising an antiferromagnet with an in-plane easy spin axis. Therefore, our approach shifts the focus of enabling new material functionalities from externalities to the rational material heterostructure design. We demonstrated that multiple effects occur concurrently in the created interfaces between a monolayer semiconductor WSe_2 and an antiferromagnet $CrCl_3$ at the nanoscale: (1) spin-selective charge transfer, (2) activation of dark excitons due to in-plane proximity magnetic field, and (3) modulation of the fine structure splitting *via* Zeeman effect. Based on these findings, we propose that our $CrCl_3/WSe_2$ heterostructure can act as a multidimensional sensor of a magnetic field.

Introduction

The technology of van der Waals (vdW) assembly instigated a shift from controlling the material properties *via* external methods toward intraheterostructure functionalities. Interfacial effects play an important role in material design, since the proximity of materials with vastly different structural, chemical, optoelectronic, or magnetic properties activates novel phenomena and provides control knobs for fundamental excitations. Notable examples include Hall magnetometry in a metal that detects the magnetic state of an adjacent layer,[1] charge tunneling in vertical heterojunctions,[2] or electronic and/or excitonic spin polarization induced by spin splitting in the presence of a

[a] *Institute of Experimental Physics, Faculty of Physics, University of Warsaw, 02-093 Warsaw, Poland. E-mail: lucja.kipczak@fuw.edu.pl, maciej.molas@fuw.edu.pl*
[b] *Institute for Functional Intelligent Materials, National University of Singapore, 117544, Singapore. E-mail: msemaci@nus.edu.sg*
[c] *Department of Materials Science and Engineering, National University of Singapore, 117575, Singapore*
[d] *Guangxi Key Laboratory of Information Materials, Guilin University of Electronic Technology, Guilin 541004, China*
[e] *Research Center for Electronic and Optical Materials, National Institute for Materials Science, 1-1 Namiki, Tsukuba 305-0044, Japan*
[f] *Research Center for Materials Nanoarchitectonics, National Institute for Materials Science, 1-1 Namiki, Tsukuba 305-0044, Japan*
[g] *School of Advanced Materials, Shenzen Graduate School, Peking University, 518055 Shenzen, China. E-mail: chenzl-cnc@pku.edu.cn*

† Electronic supplementary information (ESI) available. See DOI: https://doi.org/10.1039/d5nh00198f

‡ These authors contributed equally to this work.

Open Access Article. Published on 01 2025. Downloaded on 2026/5/15 03:53:08.
This article is licensed under a Creative Commons Attribution 3.0 Unported Licence.

proximity magnetic field (PMF).[3–6] In the domain of two-dimensional materials, it was demonstrated that interfacing a monolayer (ML) of semiconducting transition metal dichalcogenide (S-TMD), *e.g.* WSe_2, with a layered ferromagnetic material, *e.g.* $CrBr_3$, can drastically modify the optoelectronic properties of the ML.[4,7–17] Although the number of materials that could strongly interact with each other at the interface is immense, we only know a sparse representation of assembly rules leading to functionalities created *via* such a methodology.

Herewith, we demonstrate that the proximity between a $CrCl_3$[18–22] antiferromagnet with an in-plane easy-axis magnetization and a non-magnetic WSe_2 ML semiconductor leads to two distinct effects. The first one results in the quenching of the WSe_2 emission due to an efficient charge transfer process enabled by the relative alignment of the bands within the structures. The second one reveals a brightening of dark excitons without the application of an external planar magnetic field. The transparency of $CrCl_3$ crystal in the energy range of the excitonic resonances in WSe_2 ML, combined with the encapsulation with hexagonal boron nitride (hBN), enabled inspection of the photoluminescence (PL) spectra measured in the series of the $WSe_2/CrCl_3$ heterostructures. The formation of the structures results in quenching of multiexcitonic emission in WSe_2 ML,[23–37] driven by a charge transfer process enabled by the relative band alignment within $WSe_2/CrCl_3$ heterostructure, which was confirmed by theoretical calculations. At specific locations in the structures, we observed the formation of PL spectra dominated by two narrow resonances, which were ascribed to the gray and dark exciton states in the WSe_2 ML.

The relative contribution of the dark exciton state to the gray exciton emission allowed us to estimate the in-plane component of the magnetic field, while the fine-structure splitting of the gray/dark excitons, modified by the Zeeman effect, provided an accurate value of the out-of-plane component. Our analysis demonstrated that at the locations of the strongest enhancement of the gray and dark exciton states, there existed a canted magnetization in the degree range of 10°–30° with respect to the WSe_2 ML, which we attributed to the three-dimensional topography structures naturally appearing at van der Waals interfaces. Such topography structures and their associated magnetic response were visualized by a combination of atomic and magnetic force microscopy.[38] Although $CrCl_3$ is established to be characterized by in-plane intralayer magnetization with the Curie temperature (T_C) of about 17 K,[39] the presence of out-of-plane orientation of the $CrCl_3$ magnetization with the $T_C \approx 40$ K is revealed on the deformed region of the $CrCl_3$ flake using the magnetic force microscopy (MFM).

Inspection of the optoelectronic properties of $hBN/WSe_2/CrCl_3/hBN$ heterostructures demonstrates that the technological advantages of gray and dark excitons could be intrinsically accessed through material design. This was possible through a synergistic design of vdW interfaces, combining proximity fields from an antiferromagnet, charge transfer through the relative band alignment, and suppression of dielectric inhomogeneities provided by an atomically flat insulator.

Results

We inspected the optical response of three $hBN/WSe_2/CrCl_3/hBN$ heterostructures (HSs), referred to as HS1, HS2, and HS3, created *via* mechanical exfoliation and stacking of consecutive layers. HS1 and HS2 were fabricated using the same procedure, so there is no significant difference between them, whereas HS3 was produced using the same methodology with the addition of a 2 nm hBN spacer between $CrCl_3$ and WSe_2 layers (see the Methods section for details). The hBN encapsulation enables inspection of spectrally narrow resonances, characterized by various charge states, spin/subband contribution, and/or phonon-replicated resonances, that form a family of excitonic species within WSe_2 ML.[34,35] The detailed characteristics of the excitonic response are unveiled at low temperature and are strongly dependent on the HS architecture. In our designs, the overlap of consecutive layers in HS creates three types of hBN-encapsulated areas: $hBN/CrCl_3/hBN$, $hBN/WSe_2/hBN$, and $hBN/WSe_2/CrCl_3/hBN$. This allows us to study the optical response of individual materials and HS in a comparative manner. The corresponding low-temperature (T = 5 K) PL spectra measured on HS1 are presented in Fig. 1.

The PL spectrum of the $CrCl_3$ flake shows a broadband optical response distributed from about 1.25 eV to almost 1.60 eV, which is similar to those previously reported.[40] This type of emission is typical for Cr-based trihalides of the chemical formula CrX_3 (X = Cl, Br, I) due to the emergence of Frenkel-type excitons.[41,42] CrX_3 emission spectra can be interpreted in the regime of large Huang–Rhys factors when considering a one-dimensional Franck–Condon model.[43] This means that the oscillator strength for the zero-phonon line is negligible, while the series of its phonon[44] replicas form a broad emission band. The PL spectrum for encapsulated WSe_2 ML displays several emission lines that have been attributed to recombination pathways of different excitonic species.[23–37] The detailed attribution of all emission lines is described in Section S1 of the ESI,† while here we focus on the two emission lines of interest that drive the functionality of our HS. These two resonances, denoted X^B and X^G, are attributed to neutral bright and gray excitons composed of carriers from the $K^{\pm}$ points of the Brillouin zone (BZ),[45,46] respectively.

For the $hBN/WSe_2/CrCl_3/hBN$ HS2, which PL spectra are analyzed in Section S2 of the ESI,† we observed a quenching of the total spectrally-integrated PL intensity from the WSe_2 ML by a factor of about 18. The quenching is so robust that the WSe_2 PL signal from the majority of the $WSe_2/CrCl_3$ HS area is negligible. Furthermore, the shape of the PL spectra measured on the $hBN/WSe_2/CrCl_3/hBN$ HS2, formed by single broad peaks centered at about 1.7 eV, is completely different from the one of WSe_2 ML, compare Fig. S2 and S3 in the ESI.† The variations in the optical response of WSe_2 ML under different environmental conditions were visualized using spatially-resolved emission mapping realized on $hBN/WSe_2/hBN/CrCl_3/hBN$ HS3 as illustrated and discussed in Sections S3 and S4 of the ESI.† In the HS3, the hBN spacer was added between the WSe_2 and $CrCl_3$ layers, which is partially present within the HS

 This journal is © The Royal Society of Chemistry 2025

Open Access Article. Published on 01 2025. Downloaded on 2026/5/15 03:53:08.
This article is licensed under a Creative Commons Attribution 3.0 Unported Licence.

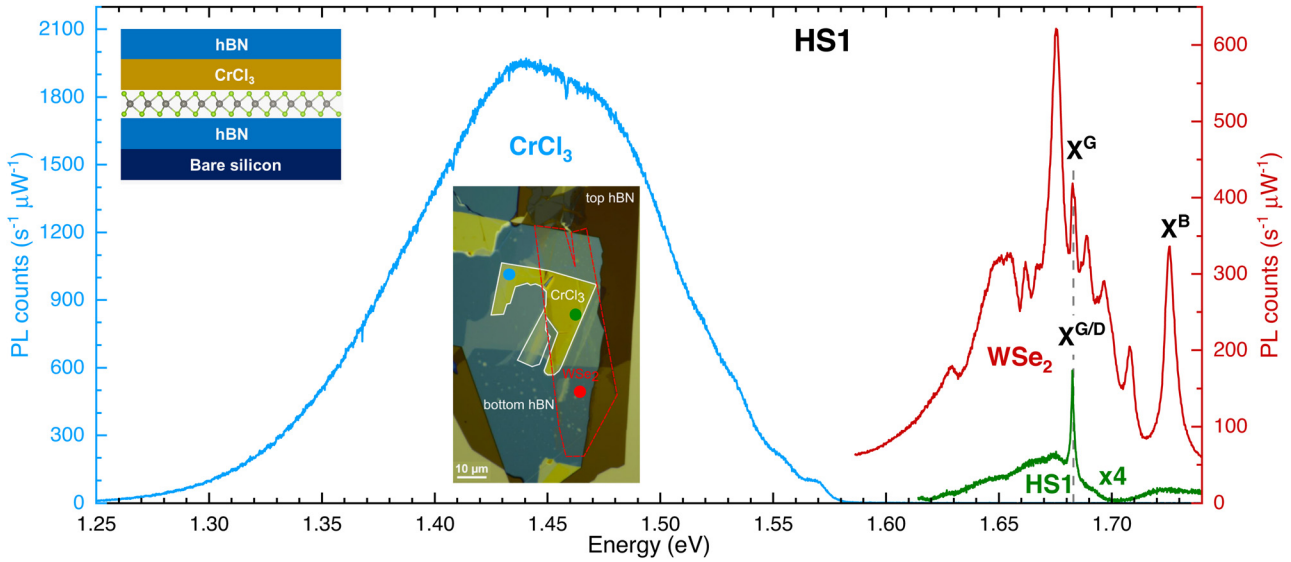

Fig. 1 Photoluminescence spectra of three structures: hBN/$CrCl_3$/hBN with thick $CrCl_3$ flake (blue), a hBN/WSe_2/hBN with WSe_2 monolayer (red) and heterostructure hBN/WSe_2/$CrCl_3$/hBN (green) measured on the sample referred to as HS1 at low temperature (T = 5 K), using excitation energy 2.41 eV and laser power of 15 W. The spectra are vertically shifted or multiplied by the scaling factor for clarity. The inset in the top-left corner shows the schematic side view of the sample with the indication of consecutive layers. The inset in the central part of the figure demonstrates the optical image of the heterostructure. The outlines for the individual flakes are added as a guide for the eye. The colored dots in the optical image indicate spatial positions corresponding to the photoluminescence spectra of different material configurations.

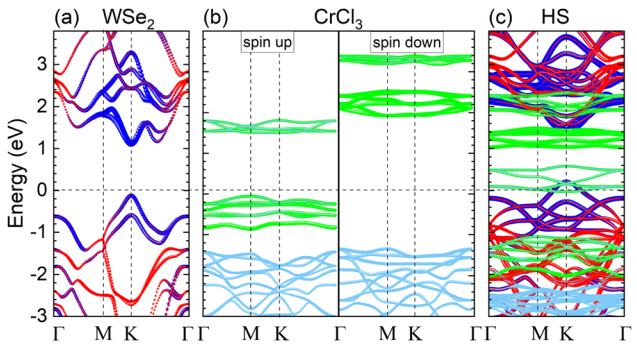

Fig. 2 The element-projected band structure of (a) WSe_2 monolayer, (b) $CrCl_3$ ML, and (c) WSe_2/$CrCl_3$ heterostructure. The atomic projection is color-coded as follows: W (blue), Se (red), Cr (light-blue), and Cl (light-green). In the heterostructure (HS) case, the lattice of WSe_2 monolayer was stretched to match the Brillouin zone high symmetry points between both materials for ease of comparison.

area, providing a varied degree of the WSe_2 and $CrCl_3$ interfacial coupling in the same sample. To understand the mechanism behind the quenching of the WSe_2 PL intensity that occurred most robustly in the case of the direct WSe_2/$CrCl_3$ interface, we investigated the relative band alignment between bulk $CrCl_3$ and WSe_2 ML through density functional theory (DFT) at the level of single-particle PBE functional (see the Methods section for computational details). Atom projected band structures for WSe_2 ML, $CrCl_3$ ML, and $CrCl_3$/WSe_2 HS are presented in Fig. 2. The direct band gap at the K point of the BZ for WSe_2 ML was reproduced in our calculations with the electronic states around the band edges composed mainly of the d-type orbitals of tungsten. Spin–orbit splitting of the maximum of the valence band was found from first principles to yield 469 meV, consistent with previous calculations using the same level of functional.[47]

In the case of $CrCl_3$, the edges of the electronic bands are predominantly composed of the d-type orbitals of the chromium atoms. Due to the atomic localization of the excitons and consequently weak confinement effects, calculations were done for $CrCl_3$ ML. The nearest–neighbor Cr–Cr spin exchange results in significant splitting of the opposite spin subbands, arising from the ferromagnetic nature of $CrCl_3$. The magnetic moment per Cr atom, responsible for the emergence of net magnetization, was calculated to be equal to 3.0 μ_B (μ_B is the Bohr magneton).

The formation of $CrCl_3$/WSe_2 HS and the inspection of its electronic properties using DFT methods are non-trivial, as the materials exhibit a large difference in lattice constant. Therefore, in terms of the absolute values of the momentum, the K points in both materials are strongly displaced. However, since the $CrCl_3$ bands are flat given the strong contribution of the d-type orbitals of the heavy transition metal atoms, the momentum mismatch does not lead to significant energy modifications in plausible charge transfer processes. Therefore, we have stretched the WSe_2 lattice to achieve comparable unit cells for ease of comparison. Under such assumptions, we obtained a band structure of WSe_2 ML and $CrCl_3$ ML HS, see Fig. 2(c). The relative position of the band edges is determined by the difference in work function that characterizes both materials individually. We have calculated that the work function is equal to 6.17 eV for bulk $CrCl_3$ and 5.10 eV for WSe_2 ML. Therefore, based on our calculations and determined work functions, the HS exhibits a type-II band alignment.

Open Access Article. Published on 01 2025. Downloaded on 2026/5/15 03:53:08.
This article is licensed under a Creative Commons Attribution 3.0 Unported Licence.

Specifically, the occupied valence band of $CrCl_3$ lies below the valence band of WSe_2 ML, while the unoccupied conduction band of $CrCl_3$ is positioned above the valence band of WSe_2 ML, within the band gap of WSe_2. From this result, we expect a tendency to transfer electrons from WSe_2 to $CrCl_3$. Indeed, from the band structure of the $CrCl_3/WSe_2$ HS, we can observe that the spin-up conduction band edge in $CrCl_3$ is located within the top of the ML WSe_2 valence band. Such an arrangement of the subbands leads to depopulation of the WSe_2 valence band in favor of doping the $CrCl_3$ conduction band, preventing intra-WSe_2 optical excitations. Photoexcited electron–hole pairs involving higher-energy subbands are also likely to undergo recombination/relaxation through channels involving states in $CrCl_3$ at a level of excited and ground exciton states. Therefore, we associate the observed quenching of PL in ML WSe_2 with the charge transfer from WSe_2 to $CrCl_3$.

As vdW interfaces are rarely perfect, we can identify individual scarce locations at examined HSs, when quenching is notably suppressed. At these particular locations, the character of the WSe_2 ML spectrum is drastically altered, compared to the typical PL measured in the HS (compare Fig. S2 and S3 in the ESI†). The PL spectrum becomes dominated by a single resonance at an energy of 1.68 eV, akin to the PL spectra observed in a large in-plane magnetic field.[32] The emission energy and linewidth of this resonance in $WSe_2/CrCl_3$ HS is the same as in WSe_2 ML encapsulated in hBN inspected in previous reports, demonstrating that the WSe_2 ML in the $hBN/WSe_2/CrCl_3/hBN$ HS remains unstrained. Therefore, we conclude that the origin of this type of spectra is related to the features of interfacial van der Waals topography, such as bubbles or wrinkles occurring in the $CrCl_3$ layer, which can lead to the suppression of the efficiency of the charge-transfer mechanism. We attribute the narrow resonance to the neutral gray/dark excitons state ($X^{G/D}$) activated by the in-plane component of the PMF from the planar ferromagnet.

To verify our attribution of the $X^{G/D}$ line, we performed polarization-resolved measurements of the two similar $X^{G/D}$ lines identified for HS1 and HS2. Fig. 3(a) and (b) show the PL spectra of the $X^{G/D}$ lines recorded for two orthogonal linear polarizations. The energy of the $X^{G/D}$ resonances differed by 5.4 meV between the HS1 and HS2 samples, consistent with the variation in the gray/dark excitons energy reported in the literature.[23–37] This difference can be ascribed to the modifications in excitonic energy in S-TMD ML originating predominantly from the inhomogeneities of the dielectric environment, in particular the thickness of the surrounding layers: bottom hBN flake and top $CrCl_3$ flake.[48] We found that the $X^{G/D}$ line is characterized by two linearly polarized components. It is important to point out that the polarization properties of the $X^{G/D}$ lines shown in Fig. 3(a) and (b) are different. The angles between the X^D and X^G signals differ for HS1 and HS2, respectively. The absolute values of the polarization angles depend on the alignment of the optical setup with respect to the orientation of the WSe_2 flake. Notably, the difference between the two components equaled exactly 90°, providing information about the orthogonal alignment of the two linearly

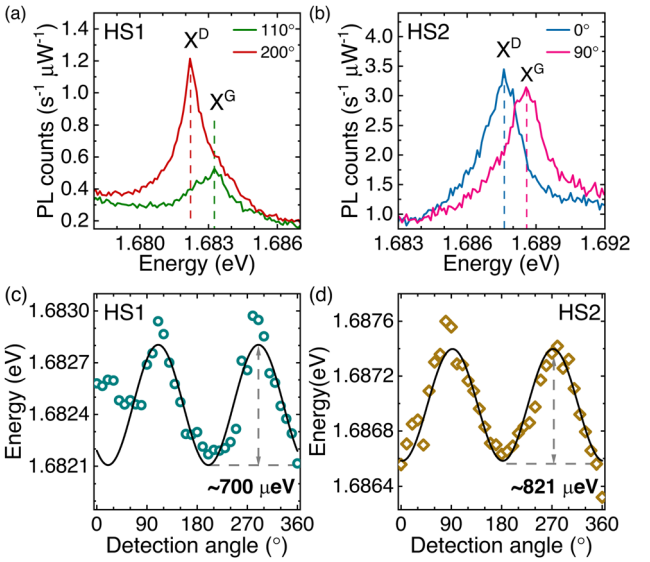

Fig. 3 Low temperature (T = 5 K) photoluminescence spectra of the gray/dark exciton resonance ($X^{G/D}$) recorded for two orthogonal linear polarizations measured for two $hBN/WSe_2/CrCl_3/hBN$ heterostuctures (HS): (a) HS1 and (b) HS2. The corresponding linear polarization dependence of the gray/dark exciton energy is presented for (c) HS1 and (d) HS2 samples. The solid black curves demonstrate the results of the least square fitting method using eqn (1).

polarized resonances. Although the gray and dark exciton peaks, shown in Fig. 3(a), reveal correspondingly partial and full linear polarizations, in line with the previous results for the WSe_2 ML under an in-plane magnetic field,[32] the polarization properties of the analogous features in Fig. 3(b) display almost full linear polarization. These results can be explained by the presence of not only the in-plane component of PMF but also the out-of-plane PMF, which should lead to conversion from linear to circular polarization of the gray/dark excitons lines through the intermediate cases characterized by elliptical polarization (see ref. 32 for details). The estimated out-of-plane component of the magnetic field in HS2 (see the Discussion section) is larger than in HS1, in agreement with different polarization properties of the $X^{G/D}$ lines in both HSs as the polarization of the $X^{G/D}$ emissions changes from the linear ones at zero field to the circular ones in high magnetic fields. The evolution of the $X^{G/D}$ emission energy with the detection angle, $E(\theta)$, is shown in Fig. 3(c) and (d). Due to the limited spectral resolution of our experimental setup, we deconvoluted the PL spectra shown in Fig. 3(a) and (b) using a single Lorentzian function. The change in energy as a function of the polarization angle indicates that the emission line consists of two components, which we identify as X^G and X^D. The angle dependence of the $X^{G/D}$ energy can be analyzed using a formula that reads

$$E(\theta) = E_0 + \Delta \cos^2(\theta - \phi), \quad (1)$$

where E_0 and ϕ are the fitting parameters that describe energy and phase, while Δ represents the energy separation between two linearly polarized components of $X^{G/D}$. The fitted curves are shown in Fig. 3(c) and (d). The Δ values were 700 ± 112 eV for

 This journal is © The Royal Society of Chemistry 2025

Open Access Article. Published on 01 2025. Downloaded on 2026/5/15 03:53:08.
This article is licensed under a Creative Commons Attribution 3.0 Unported Licence.

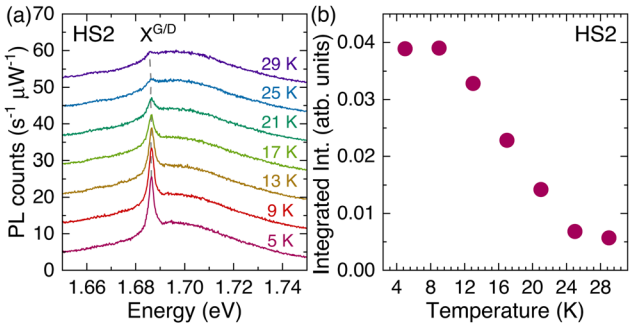

Fig. 4 (a) The temperature dependent photoluminescence spectra of the hBN/WSe_2/$CrCl_3$/hBN heterostructure (HS2) in range of temperatures 5–29 K. Spectra were shifted vertically for clarity. (b) The integrated intensity of the gray/dark exciton $X^{G/D}$ resonance is shown as a function of temperature.

HS1 and 820 ± 105 eV for HS2. The polarization dependence and two-component structure are qualitatively consistent with previous analysis of the polarization properties of $X^{G/D}$ in the presence of the in-plane magnetic field. However, the value of the splitting is enhanced in our structures.

To conclude our observations, we verified the origin of the gray/dark exciton brightening by inspecting the temperature dependence of its intensity, see Fig. 4(a) and (b). The $X^{G/D}$ feature disappears monotonically with increasing temperature until it is no longer discernible at a temperature of about 30 K. This obtained temperature is almost two times higher than the reported Curie temperature characterizing the intraplane magnetization coupling in $CrCl_3$ (17 K[39]), which can be attributed to the strain and/or stacking faults[49] in the ferromagnetic layer instigated by the topography features of the heterostructure.[50] This observation is consistent with previous demonstration of elevated Curie temperature in $CrBr_3$ bubbles,[51] which form as a result of the heterostructure assembly using polymer membranes.[52] The increase in Curie temperature in $CrCl_3$ due to its inhomogeneity is discussed in detail below. The observation of the $X^{G/D}$ state constitutes evidence of the presence of the in-plane component of a magnetic field in the WSe_2 ML, which in the HS can only originate from the in-plane magnetization of the $CrCl_3$ layer.

Discussion

The intravalley K exciton composed of carriers that occupy the edge of the spin–orbit-split bands is characterized by the opposite spin of electrons and holes in WSe_2 ML.[32,34,35,53] These kind of bound electron–hole pairs are known as spin-forbidden neutral dark excitons. The spin–spin exchange interaction gives rise to the double (fine) structure comprising the so-called gray and dark excitons,[53–56] which are qualitatively different. The gray exciton has an optically active recombination channel with photons emitted within the plane of the ML.[55] This exciton can be observed in standard out-of-plane configurations when using objectives with a high numerical aperture, in the absence of a magnetic field.[32,53,57] The dark exciton state is truly optically forbidden, and its activation requires a magnetic field, which leads to mixing of intervalley states with opposite spins (out-of-plane configuration of the applied magnetic field)[53] or admixture of bright states into dark ones (in-plane arrangement of the external magnetic field).[45] Consequently, the oscillator strength is inherited from the gray exciton or bright exciton, respectively. The exchange interactions give rise to a fine structure energy splitting between the gray and dark excitons, which are active in mutually orthogonal linear polarizations.[32,54,55,58] Our zero-field polarization-resolved inspection of the narrow resonance in the $CrCl_3$/WSe_2 HS indicates that we observe both gray and dark exciton states. The temperature dependence performed for the gray/dark exciton demonstrates that the gray/dark exciton arises due to the PMF of the $CrCl_3$ antiferromagnet. Note that the polarization and temperature evolutions of the gray exciton emission in the WSe_2 ML are described in Sections S5 and S6 of the ESI,† respectively. Demonstration of the origin of the modification of the PL spectra of WSe_2 ML allows us to inspect the functionalities of the HS in the domain of magnetic field sensing. Firstly, the presence of the gray/dark exciton requires a strong in-plane component of the magnetic field, typically above 1 T. As the intensity of the gray and dark exciton lines increases with the magnetic field due to enhanced mixing with the bright state, the ratio of the dark exciton to the gray exciton can act as an estimation of the field component.[32] Consequently, we estimated the in-plane component of the field to yield 2.2 T ± 0.6 T for HS1 and 1.3 T ± 0.7 T for HS2, based on the comparison with the magnetic field dependence of the PL spectrum of hBN encapsulated WSe_2 ML.[32]

Our data also indicate the presence of the out-of-plane component of the magnetic field within the HS. Gray and dark excitons constitute two Zeeman-split branches with a zero-field anticrossing originating from the exchange coupling.[32,53] Therefore, the evolution of the energy of both resonances in an out-of-plane magnetic field can be described by the formula:

$$E_{G/D} = E_0 \pm \frac{1}{2}\sqrt{\Delta^2 + (g\mu_B B_\perp)^2}, \quad (2)$$

where E_G and E_D are the energies of the gray and dark excitons corresponding to the + and − signs, respectively. Δ is the zero-field splitting between the gray and dark excitons, g denotes the g-factor, and $B_\perp$ is the value of the out-of-plane magnetic field.

Using the experimental data reported in the literature for WSe_2 MLs encapsulated in hBN flakes, we calculated average values of Δ = 637 ± 200 eV[32,53] and g = 9.4 ± 0.4.[30–32,35,37,53,59–61] Finally, by reformulating eqn (2), we obtained $B_\perp$ = 0.53 ± 0.12 T for HS1 and $B_\perp$ = 0.95 ± 0.10 T for HS2.

Our methodology of determining the in-plane and out-of-plane components of the PMFs enables simultaneous sensing in two dimensions, obtaining the planar and perpendicular field components with respect to the WSe_2 ML plane. We found canted orientations of the proximity field that yield 13.5° ± 1.1° for HS1 and 36.1° ± 1.9° for HS2. We expect that our observations are enabled by topography features in the $CrCl_3$ layer,

Open Access Article. Published on 01 2025. Downloaded on 2026/5/15 03:53:08.
This article is licensed under a Creative Commons Attribution 3.0 Unported Licence.

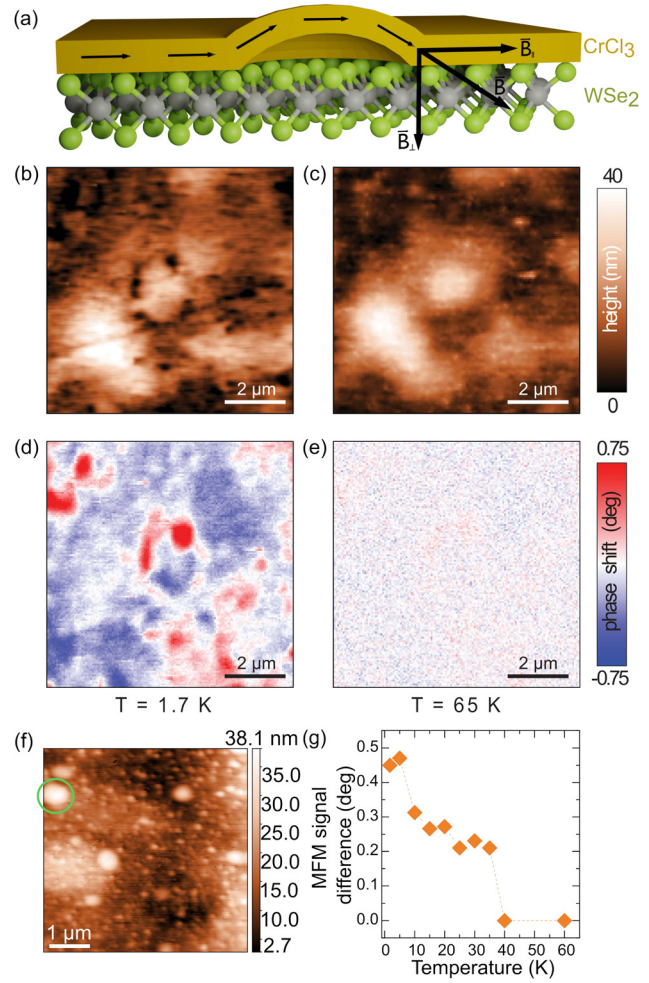

Fig. 5 (a) Simplified side view scheme of the $CrCl_3/WSe_2$ heterostructure. The $CrCl_3$ flake is denoted by the yellow layer, and the gray and green balls depict to the W and Se atoms, respectively. The $\vec{B}$ represents the orientation of the effective proximity magnetic field propagating from the $CrCl_3$ layer to the WSe_2 ML. $\vec{B}_\parallel$ and $\vec{B}_\perp$ correspond the decomposition of the $\vec{B}$ field into the in-plane and out-of-plane components. (b) and (c) AFM images of the topography scans of the $CrCl_3/WSe_2$ sample surface obtained at T = 1.7 K and T = 65 K, correspondingly. (d) and (e) MFM images of the same area as in (b) and (d), measured at zero magnetic field with the lifted hight of 200 nm. (f) AFM images of the topography of the exfoliated $CrCl_3$ flake where the intraplane Curie temperature was measured on the bubble, marked by the green circle. (g) Temperature dependence of the magnetic force microscopy (MFM) signal difference extracted for the bubble marked in panel (f).

based on the analysis of the PL intensity quenching mechanism, the localized nature of the brightening spots for the gray/dark excitons, and the canted orientations of the proximity field. A simplified schematic of the $CrCl_3/WSe_2$ structure in the vicinity of the locations with gray/dark excitons' narrow emissions is demonstrated in Fig. 5(a). The $CrCl_3$ bubble causes substantial weakening of the quenching effect and simultaneously the brightening effect of the gray/dark excitons owing to both the in-plane and out-of-plane components of the PMF. The non-zero net magnetization in $CrCl_3$ arises intrinsically in an odd number of layers, where ferromagnetic monolayers are coupled *via* antiferromagnetic interlayer exchange interactions. The net magnetization in the absence of an external magnetic field may be further enhanced due to the presence of commonly observed stacking faults,[49,62–64] which can change the character of the interlayer coupling from antiferromagnetic to ferromagnetic. The frequent emergence of the stacking faults is attributed to minuscule structural energy differences calculated for different stacking configurations,[49] which are therefore even more probable to occur in the presence of perturbed topography. The $CrCl_3$ bubble areas should be characterized by a canted magnetization in conjunction with enhanced PMF values.

Consequently, the observed effect is expected to be restricted to the specific positions of the investigated heterostructures, as previously presented. To verify these assumptions, we inspected the structural topography and spatially resolved magnetic response of the HS3 using atomic force microscopy (AFM) and magnetic force microscopy (MFM), respectively. The results of the imaging are illustrated in Fig. 5(b)–(d). Here, we focused on a bubble feature characterized by a diameter of about 2 m, which constitutes a common feature in the topography. The estimations of strain based on the curvature of typical bubbles yield values in the range of 0.03–0.08%, of the similar order as bubbles investigated previously in $CrBr_3$ films.[51] The magnetic signal clearly demonstrated a strong out-of-plane magnetic field component at the base of the bubble, where the curvature of the bubble is the largest, while the interfacial proximity between the antiferromagnet and semiconductor can maintain the charge transfer mechanism. Although the topography of the heterostructure is not substantially affected by the change of temperature from 1.7 K to 65 K, the corresponding magnetic response completely vanished at T = 65 K, see Section S7 of ESI† for details. In order to verify the influence of the topographic features, we performed detailed MFM measurements in the sample region characterized by bubbles. Fig. 5(f) presents the topography of the particular region measured on the $CrCl_3$ flake, where several bubbles of different sizes are observed. The green circle marks the bubble chosen for the examination of the MFM signal as a function of the temperature, which is concluded in Fig. 5(g). The systematic characterization of the magnetic response using the MFM signal difference is discussed in Section S8 of the ESI.† Within the temperature range of 1.7 to 40 K, a decrease in the MFM signal is clearly observed with no magnetic response detected at 40 K. This confirms previous theoretical calculations[50] that the strain leads to significant growth of the intraplane T_C value in $CrCl_3$ from 17 K for unstrained material[39] to about 40 K, as is determined for the particular bubble. The discrepancy between the values of the Curie temperatures obtained using the temperature analysis of the dark/gray exciton emissions ($T_C \approx$ 30 K) and the MFM signal ($T_C \approx$ 40 K) can be explained in terms of various geomteries characterizing bubbles within the same sample. The observed magnetic inhomogeneity at T = 1.7 K and the elevated intraplane Curie temperature found in the particular bubble confirmed the local character of the $X^{G/D}$ emission. These findings explain the rare occurrence of

 This journal is © The Royal Society of Chemistry 2025

Open Access Article. Published on 01 2025. Downloaded on 2026/5/15 03:53:08.
This article is licensed under a Creative Commons Attribution 3.0 Unported Licence.

gray/dark exciton brightening, which requires an appropriate combination of magnetic and electronic proximity effects while maintaining the high quality of the sample manifested as narrow excitonic lines.

The focal inquiry pertains to the underlying mechanism responsible for the observed magnetic proximity field. Experimental reports indicate that the strength of magnetic proximity interactions (MPI) exhibited by an effective magnetic field that influences S-TMD MLs is typically around 10 T for magnetic layers with out-of-plane easy-axis magnetization.[6,8,9,13] It is well established that MPI requires a pristine interface between magnetic and non-magnetic substances. Alternatively, diffuse magnetic fields can also serve as a source of proximity fields, however, the effects on charge carriers within the interfaced semiconductor were found only on the order of tens of mT.[65] Given the measured values of the magnetic proximity field of about 1 T in both directions strongly suggest the presence of MPI. These values are an order of magnitude smaller than those of structures characterized by out-of-plane magnetization and a clean interface between magnetic and nonmagnetic materials. On the basis of our AFM and MFM characterization, we found that the conditions for gray/dark exciton brightening are most likely met around the perimeters constituting the base of the $CrCl_3$ bubbles, where the angle of magnetic field canting and strain effects are the largest,[52] with minimal electronic decoupling between the two materials enabling perseverance of MPI. The last important issue to be discussed is the significant suppression of the charge transfer effect allowing observation of the dark exciton emission. As the lifetime of the bright neutral exciton is only about a few picoseconds and the decay of the dark neutral exciton extends to hundreds picoseconds,[53] the charge transfer should be much more efficient for the $X^{D/G}$ emission than for the X^B one. This discrepancy can be explained by two possible effects: (i) the magnitude of the in-plane MPF is so strong that it brightens the dark exciton emission similarly to the case of the external in-plane magnetic field influence reported for the WSe_2 ML.[32] Consequently, the $X^{D/G}$ intensity is significantly higher compared to the X^B intensity, resulting in the observation of dark exciton emission. (ii) the charge transfer between WSe_2 ML and $CrCl_3$ is spin dependent. The difference between bright and dark excitons in WSe_2 ML comes from the different spin orientation of an electron that forms a given excitonic complex. As can be seen in Fig. 2, the bands with spin up are characterized by much smaller energies than those with spin down, which may result in more favorable charge transfer for X^B species than for the X^D ones. Consequently, the charge transfer for the dark complexes is suppressed, which allows us to observe its emission. Such spin-dependent charge transfer was recently reported for the $MoSe_2/CrBr_3$ heterostructures.[14,17]

Summary

In summary, we have demonstrated a ferromagnetic proximity effect within $hBN/WSe_2/CrCl_3/hBN$ heterostructures, which led to the development of multidimensional detection of magnetic fields by inspection of a gray/dark exciton state. A photoluminescence quenching mechanism *via* intermaterial charge transfer enabled us to isolate individual locations within the heterostructure, where the spectra are dominated by a brightened gray/dark exciton state under zero-external-field conditions. The appearance of the out-of-plane orientation of the $CrCl_3$ magnetization with the elevated intraplane Curie temperature of 40 K was established on the distorted region of the sample using the magnetic force microscopy. This finding unlocks the potential opportunity to control the Curie temperature using topography features and to utilize long-lived gray and dark states for synergistic optoelectronic and sensing applications *via* design of quantum material heterostructures.

Methods

Samples

The $CrCl_3$ and WSe_2 crystals, used for the preparation of the investigated samples, were purchased from HQ graphene. Thin $CrCl_3$ and monolayer WSe_2 flakes were exfoliated directly on 285 nm SiO_2/Si substrates in an inert gas glovebox (O_2 < 1 ppm, H_2O < 1 ppm). Then we used a poly (bisphenol A carbonate)/polydimethylsiloxane stamp on a glass slide to pick up thin hBN with thickness below ~10 nm, ~10–20 nm $CrCl_3$, monolayer WSe_2, 50 nm hBN at 80 °C with the assistance of the transfer stage in the glove box. The hBN encapsulation limited the degradation of $CrCl_3$ layers.[66] Moreover, we intentionally placed the WSe_2 ML directly on the bottom hBN layer in order to obtain high quality layer and spectrum of the WSe_2 ML. This approach is based on the well-established observation that the hBN encapsulation improves the quality of TMDs ML.[67–69] Finally, the stack was released on a fresh silicon substrate without additional layers of oxides. The HS1 and HS2 structures are characterized by the same stacking order (from bottom to top) hBN/WSe_2 ML/$CrCl_3$/hBN. The sample studied in the MFM experiment, *i.e.* HS3, was modified compared to the above ones by adding an extra thin hBN spacer between $CrCl_3$ and WSe_2 ML, hence the structure was deposited on etched silicon with enhanced roughness. Due to the used exfoliation procedure, the thicknesses of the bottom and top hBN flakes and $CrCl_3$ can be subjected to variation up to a single tens of nanometers. The thicknesses of the flakes were first identified by optical contrast and then more precisely measured with an atomic force microscope.

Photoluminescence experiments

PL measurements were performed with the samples placed on a cold finger of a continuous-flow cryostat. Measurements were taken at a low temperature of T = 5 K and as a function of temperature from T = 5 K to 60 K using a λ = 515 nm (2.41 eV) diode laser. The excitation light was focused by means of a 50× long-working-distance objective with a 0.55 numerical aperture (NA) producing a spot of about 1 μm diameter. The signal was collected *via* the same objective (back-scattering

Open Access Article. Published on 01 2025. Downloaded on 2026/5/15 03:53:08.
This article is licensed under a Creative Commons Attribution 3.0 Unported Licence.

geometry), sent through a 0.75 m monochromator, and then detected using a liquid nitrogen-cooled charge-coupled device (CCD). The polarization-resolved PL spectra were analyzed by a motorized half-wave plate and a fixed linear polarizer mounted in the detection path.

Atomic and magnetic force microscopies

AFM and MFM were performed using an attocube attoDRY 2100 closed-cycle cryogenic microscope with a base temperature of 1.7 K, equipped with a 9 T superconducting magnet. Nanosensors PPP-MFMR silicon probes with magnetic CoCr-coating, spring constant k = 2.8 N m^{-1}, and resonance frequency of ~75 kHz was used. Prior to the measurements, the probe was magnetized at room temperature using a neodymium magnet. In the MFM data, magnetic contrast was observed in both tapping and non-contact lift modes in the phase signal at 1.7 K. In the non-contact regime, the cantilever was held at a constant height (lift) from 50–500 nm depending on the type of experiment. To take into account the topography of the sample surface, MFM measurements were conducted in dual pass mode.

Theoretical calculations

Our calculations are based on DFT using the PBE functional implemented in the Vienna Ab Initio Simulation Package (VASP).[70–72] The interaction between valence electrons and ionic cores is described within the projector augmented (PAW) approach with a plane-wave energy cutoff of 500 eV.[73] Spin polarization was included in all calculations. Dispersion forces were accounted for in our calculations using the Grimme DFT-D2 method.[74] At this level, the interlayer spacing between $CrCl_3$ and WSe_2 was optimized to be 3.51 Å. The lattice constant for $CrCl_3$ and WSe_2 is 6.06 Å and 3.17 Å, respectively. Due to the lattice mismatch between the crystals, a large moiré period should be expected for the interfaces of the two materials. The simulation of such full-scale moiré heterostructure generally exceeds the ability to perform DFT calculations due to the large supercell and computational consumption. Herein, we constructed the $CrCl_3/WSe_2$ heterostructure by combining a $(1 \times 1 \times 1)$ $CrCl_3$ and a $(2 \times 2 \times 1)$ WSe_2. The BZ was sampled using a $(7 \times 7 \times 1)$ Monkhorst–Pack grid. A 20 Å vacuum space was used to avoid interaction between neighboring layers. In structural energy minimization, the atomic coordinates are allowed to relax until the forces on all atoms are less than 0.01 eV Å^{-1}. The energy tolerance is 10^{-6} eV.

Author contributions

Ł. K., M. G., A. B., M. K. and M. R. M. performed the photoluminescence experiments. S. G. carried out the investigations using the magnetic force microscopy. Z. C. and K. V. fabricated the studied samples. P. H. carried out the DFT calculations. K. W. and T. T. grew the hBN crystals. M. R. M. initiated and supervised the project. Ł. K., M. G., S. G., P. H., M. K. and M. R. M. wrote the manuscript with inputs from all co-authors.

Conflicts of interest

The authors declare no competing interests.

Data availability

The data that support the findings of this work are available from the corresponding authors upon reasonable request.

Acknowledgements

The authors thank Tomasz Badalski for helping with the preparation of the figure presenting the side view scheme of the $CrCl_3/WSe_2$ heterostructure. The work was supported by the National Science Centre, Poland (grant no. 2020/37/B/ST3/02311), the Ministry of Education (Singapore) through the Research Centre of Excellence program (grant EDUN C-33-18-279-V12, I-FIM) and under its Academic Research Fund Tier 2 (MOE-T2EP50122-0012), and the Air Force Office of Scientific Research and the Office of Naval Research Global under award number FA8655-21-1-7026. P. H. thanks the support of the National Key Research and Development Program (no. 2021YFB3802400) and the National Natural Science Foundation (no. 52161037) of China. K. W. and T. T. acknowledge support from the JSPS KAKENHI (grant numbers 21H05233 and 23H02052) and World Premier International Research Center Initiative (WPI), MEXT, Japan. The computational work is performed on computational resources at the National Supercomputing Center of Singapore (NSCC) and the NUS HPC.

References

1 K. S. Novoselov, S. V. Morozov, S. V. Dubonos, M. Missous, A. O. Volkov, D. A. Christian and A. K. Geim, *J. Appl. Phys.*, 2003, **93**, 10053–10057.
2 W. L. McMillan, *Phys. Rev.*, 1968, **175**, 537–542.
3 J. J. Hauser, *Phys. Rev.*, 1969, **187**, 580–583.
4 S. K. Behera, M. Bora, S. S. Paul Chowdhury and P. Deb, *Phys. Chem. Chem. Phys.*, 2019, **21**, 25788–25796.
5 V. Voroshnin, A. V. Tarasov, K. A. Bokai, A. Chikina, B. V. Senkovskiy, N. Ehlen, D. Y. Usachov, A. Grüneis, M. Krivenkov, J. Sánchez-Barriga and A. Fedorov, *ACS Nano*, 2022, **16**, 7448–7456.
6 E.-M. Choi, K. I. Sim, K. S. Burch and Y. H. Lee, *Adv. Sci.*, 2022, **9**, 2200186.
7 Q. Zhang, S. A. Yang, W. Mi, Y. Cheng and U. Schwingenschlögl, *Adv. Mater.*, 2016, **28**, 959–966.
8 D. Zhong, K. L. Seyler, X. Linpeng, R. Cheng, N. Sivadas, B. Huang, E. Schmidgall, T. Taniguchi, K. Watanabe, M. A. McGuire, W. Yao, D. Xiao, K.-M. C. Fu and X. Xu, *Sci. Adv.*, 2017, **3**, e1603113.
9 K. L. Seyler, D. Zhong, B. Huang, X. Linpeng, N. P. Wilson, T. Taniguchi, K. Watanabe, W. Yao, D. Xiao, M. A. McGuire, K.-M. C. Fu and X. Xu, *Nano Lett.*, 2018, **18**, 3823–3828.
10 D. Ghazaryan, M. T. Greenaway, Z. Wang, V. H. Guarochico-Moreira, I. J. Vera-Marun, J. Yin, Y. Liao, S. V. Mrozov,

 This journal is © The Royal Society of Chemistry 2025

Open Access Article. Published on 01 2025. Downloaded on 2026/5/15 03:53:08.
This article is licensed under a Creative Commons Attribution 3.0 Unported Licence.

O. Kristanovski, A. I. Lichtenstein, M. I. Katsnelson, F. Withers, A. Mishchenko, L. Eaves, A. K. Geim, K. S. Novoselov and A. Misra, *arXiv*, 2018, preprint, arXiv:1803.02120 [cond-mat.mes-hall], DOI: 10.48550/arXiv.1803.02120.

11 Z. Zhang, X. Ni, H. Huang, L. Hu and F. Liu, *Phys. Rev. B*, 2019, **99**, 115441.

12 K. Zollner, P. E. Faria Junior and J. Fabian, *Phys. Rev. B*, 2019, **100**, 085128.

13 L. Ciorciaro, M. Kroner, K. Watanabe, T. Taniguchi and A. Imamoglu, *Phys. Rev. Lett.*, 2020, **124**, 197401.

14 T. P. Lyons, D. Gillard, A. Molina-Sánchez, A. Misra, F. Withers, P. S. Keatley, A. Kozikov, T. Taniguchi, K. Watanabe, K. S. Novoselov, J. Fernández-Rossier and A. I. Tartakovskii, *Nat. Commun.*, 2020, **11**, 6021.

15 M.-C. Heißenbüttel, T. Deilmann, P. Krüger and M. Rohlfing, *Nano Lett.*, 2021, **21**, 5173–5178.

16 K. Zollner, P. E. Faria Junior and J. Fabian, *Phys. Rev. B*, 2023, **107**, 035112.

17 J. Choi, C. Lane, J.-X. Zhu and S. A. Crooker, *Nat. Mater.*, 2023, **22**, 305–310.

18 W. N. Hansen and M. Griffel, *J. Chem. Phys.*, 1958, **28**, 902.

19 J. Cable, M. Wilkinson and E. Wollan, *J. Phys. Chem. Solids*, 1961, **19**, 29–34.

20 M. Gilbertini, M. Koperski, A. F. Morpurgo and K. S. Novoselov, *Nat. Nanotechnol.*, 2019, **14**, 408–419.

21 Q. H. Wang, A. Bedoya-Pinto, M. Blei, A. H. Dismukes, A. Hamo, S. Jenkins, M. Koperski, Y. Liu, Q.-C. Sun, E. J. Telford, H. H. Kim, M. Augustin, U. Vool, J.-X. Yin, L. H. Li, A. Falin, C. R. Dean, F. Casanova, R. F. L. Evans, M. Chshiev, A. Mishchenko, C. Petrovic, R. He, L. Zhao, A. W. Tsen, B. D. Gerardot, M. Brotons-Gisbert, Z. Guguchia, X. Roy, S. Tongay, Z. Wang, M. Z. Hasan, J. Wrachtrup, A. Yacoby, A. Fert, S. Parkin, K. S. Novoselov, P. Dai, L. Balicas and E. J. G. Santos, *ACS Nano*, 2022, **16**, 6960–7079.

22 C. Dai, P. He, L. Luo, P. Zhan, B. Guan and J. Zheng, *Sci. China Mater.*, 2023, **66**, 859–876.

23 E. Courtade, M. Semina, M. Manca, M. M. Glazov, C. Robert, F. Cadiz, G. Wang, T. Taniguchi, K. Watanabe, M. Pierre, W. Escoffier, E. L. Ivchenko, P. Renucci, X. Marie, T. Amand and B. Urbaszek, *Phys. Rev. B*, 2017, **96**, 085302.

24 Z. Li, T. Wang, Z. Lu, C. Jin, Y. Chen, Y. Meng, Z. Lian, T. Taniguchi, K. Watanabe, S. Zhang, D. Smirnov and S.-F. Shi, *Nat. Commun.*, 2018, **9**, 3719.

25 S.-Y. Chen, T. Goldstein, T. Taniguchi, K. Watanabe and J. Yan, *Nat. Commun.*, 2018, **9**, 3717.

26 M. Barbone, A. R.-P. Montblanch, D. M. Kara, C. Palacios-Berraquero, A. R. Cadore, D. De Fazio, B. Pingault, E. Mostaani, H. Li, B. Chen, K. Watanabe, T. Taniguchi, S. Tongay, G. Wang, A. C. Ferrari and M. Atatüre, *Nat. Commun.*, 2018, **9**, 3721.

27 M. Paur, A. J. Molina-Mendoza, R. Bratschitsch, K. Watanabe, T. Taniguchi and T. Mueller, *Nat. Commun.*, 2019, **10**, 1709.

28 E. Liu, J. van Baren, Z. Lu, M. M. Altaiary, T. Taniguchi, K. Watanabe, D. Smirnov and C. H. Lui, *Phys. Rev. Lett.*, 2019, **123**, 027401.

29 Z. Li, T. Wang, Z. Lu, M. Khatoniar, Z. Lian, Y. Meng, M. Blei, T. Taniguchi, K. Watanabe, S. A. McGill, S. Tongay, V. M. Menon, D. Smirnov and S.-F. Shi, *Nano Lett.*, 2019, **19**, 6886–6893.

30 Z. Li, T. Wang, C. Jin, Z. Lu, Z. Lian, Y. Meng, M. Blei, S. Gao, T. Taniguchi, K. Watanabe, T. Ren, S. Tongay, L. Yang, D. Smirnov, T. Cao and S.-F. Shi, *Nat. Commun.*, 2019, **10**, 2469.

31 Z. Li, T. Wang, C. Jin, Z. Lu, Z. Lian, Y. Meng, M. Blei, M. Gao, T. Taniguchi, K. Watanabe, T. Ren, T. Cao, S. Tongay, D. Smirnov, L. Zhang and S.-F. Shi, *ACS Nano*, 2019, **13**, 14107–14113.

32 M. R. Molas, A. O. Slobodeniuk, T. Kazimierczuk, K. Nogajewski, M. Bartos, P. Kapuściński, K. Oreszczuk, K. Watanabe, T. Taniguchi, C. Faugeras, P. Kossacki, D. M. Basko and M. Potemski, *Phys. Rev. Lett.*, 2019, **123**, 096803.

33 E. Liu, J. van Baren, T. Taniguchi, K. Watanabe, Y.-C. Chang and C. H. Lui, *Phys. Rev. Res.*, 2019, **1**, 032007.

34 E. Liu, J. van Baren, C.-T. Liang, T. Taniguchi, K. Watanabe, N. M. Gabor, Y.-C. Chang and C. H. Lui, *Phys. Rev. Lett.*, 2020, **124**, 196802.

35 M. He, P. Rivera, D. Van Tuan, N. P. Wilson, M. Yang, T. Taniguchi, K. Watanabe, J. Yan, D. G. Mandrus, H. Yu, H. Dery, W. Yao and X. Xu, *Nat. Commun.*, 2020, **11**, 618.

36 C. Robert, S. Park, F. Cadiz, L. Lombez, L. Ren, H. Tornatzky, A. Rowe, D. Paget, F. Sirotti, M. Yang, D. Van Tuan, T. Taniguchi, B. Urbaszek, K. Watanabe, T. Amand, H. Dery and X. Marie, *Nat. Commun.*, 2021, **12**, 5455.

37 C. Robert, H. Dery, L. Ren, D. Van Tuan, E. Courtade, M. Yang, B. Urbaszek, D. Lagarde, K. Watanabe, T. Taniguchi, T. Amand and X. Marie, *Phys. Rev. Lett.*, 2021, **126**, 067403.

38 S. Grebenchuk, C. McKeever, M. Grzeszczyk, Z. Chen, M. Śiśkins, A. R. C. McCray, Y. Li, A. K. Petford-Long, C. M. Phatak, D. Ruihuan, L. Zheng, K. S. Novoselov, E. J. G. Santos and M. Koperski, *Adv. Mater.*, 2024, **36**, 2311949.

39 M. A. McGuire, *Crystals*, 2017, **7**, 121.

40 X. Cai, T. Song, N. P. Wilson, G. Clark, M. He, X. Zhang, T. Taniguchi, K. Watanabe, W. Yao, D. Xiao, M. A. McGuire, D. H. Cobden and X. Xu, *Nano Lett.*, 2019, **19**, 3993–3998.

41 K. L. Seyler, D. Zhong, D. R. Klein, S. Gao, X. Zhang, B. Huang, E. Navarro-Moratalla, L. Yang, D. H. Cobden, M. A. McGuire, W. Yao, D. Xiao, P. Jarillo-Herrero and X. Xu, *Nat. Phys.*, 2018, **14**, 277–281.

42 S. Acharya, D. Pashov, A. N. Rudenko, M. Rösner, M. van Schilfgaarde and M. I. Katsnelson, *npj 2D Mater. Appl.*, 2022, **6**, 33.

43 M. Grzeszczyk, S. Acharya, D. Pashov, Z. Chen, K. Vaklinova, M. van Schilfgaarde, K. Watanabe, T. Taniguchi, K. S. Novoselov, M. I. Katsnelson and M. Koperski, *Adv. Mater.*, 2023, **35**(17), 2209513.

44 Ł. Kipczak, A. Karmakar, M. Grzeszczyk, R. Janiszewska, T. Woźniak, Z. Chen, J. Pawłowski, K. Watanabe, T. Taniguchi, A. Babiński, M. Koperski and M. R. Molas, *Sci. Rep.*, 2024, **14**, 7484.

45 M. R. Molas, C. Faugeras, A. O. Slobodeniuk, K. Nogajewski, M. Bartos, D. M. Basko and M. Potemski, *2D Mater.*, 2017, **4**, 021003.

Open Access Article. Published on 01 2025. Downloaded on 2026/5/15 03:53:08.
This article is licensed under a Creative Commons Attribution 3.0 Unported Licence.

46 M. Koperski, M. R. Molas, A. Arora, K. Nogajewski, A. O. Slobodeniuk, C. Faugeras and M. Potemski, *Nanophotonics*, 2017, **6**, 1289.
47 D. Le, A. Barinov, E. Preciado, M. Isarraraz, I. Tanabe, T. Komesu, C. Troha, L. Bartels, T. S. Rahman and P. A. Dowben, *J. Phys.: Condens. Matter*, 2015, **27**, 182201.
48 A. O. Slobodeniuk and M. R. Molas, *Phys. Rev. B*, 2023, **108**, 035427.
49 S. Y. Grebenchuk, M. Grzeszczyk, Z. Chen, M. Śiśkins, V. Borisov, M. Pereiro, M. I. Katsnelson, O. Eriksson, K. S. Novoselov and M. Koperski, *Adv. Sci.*, 2025, 2500562.
50 L. Webster and J.-A. Yan, *Phys. Rev. B*, 2018, **98**, 144411.
51 S. Grebenchuk, M. Grzeszczyk, Z. Chen, K. S. Novoselov and M. Koperski, *J. Phys.: Mater.*, 2024, **7**, 035009.
52 A. V. Tyurnina, D. A. Bandurin, E. Khestanova, V. G. Kravets, M. Koperski, F. Guinea, A. N. Grigorenko, A. K. Geim and I. V. Grigorieva, *ACS Photonics*, 2019, **6**, 516–524.
53 C. Robert, T. Amand, F. Cadiz, D. Lagarde, E. Courtade, M. Manca, T. Taniguchi, K. Watanabe, B. Urbaszek and X. Marie, *Phys. Rev. B*, 2017, **96**, 155423.
54 A. O. Slobodeniuk and D. M. Basko, *2D Mater.*, 2016, **3**, 035009.
55 G. Wang, C. Robert, M. M. Glazov, F. Cadiz, E. Courtade, T. Amand, D. Lagarde, T. Taniguchi, K. Watanabe, B. Urbaszek and X. Marie, *Phys. Rev. Lett.*, 2017, **119**, 047401.
56 P. E. F. Junior, K. Zollner, T. Woźniak, M. Kurpas, M. Gmitra and J. Fabian, *New J. Phys.*, 2022, **24**, 083004.
57 M. Zinkiewicz, M. Grzeszczyk, L. Kipczak, T. Kazimierczuk, K. Watanabe, T. Taniguchi, P. Kossacki, A. Babiński and M. R. Molas, *Appl. Phys. Lett.*, 2022, **120**, 163101.
58 M. Zinkiewicz, A. O. Slobodeniuk, T. Kazimierczuk, P. Kapuściński, K. Oreszczuk, M. Grzeszczyk, M. Bartos, K. Nogajewski, K. Watanabe, T. Taniguchi, C. Faugeras, P. Kossacki, M. Potemski, A. Babiński and M. R. Molas, *Nanoscale*, 2020, **12**, 18153–18159.
59 J. Förste, N. V. Tepliakov, S. Y. Kruchinin, J. Lindalu, V. Funk, M. Frög, K. Watanabe, T. Taniguchi, A. S. Baimuratov and H. Alexander, *Nat. Commun.*, 2020, **1q**, 4539.
60 E. Liu, J. van Baren, Z. Lu, M. M. Altaiary, T. Taniguchi, K. Watanabe, D. Smirnov and C. H. Lui, *Phys. Rev. Lett.*, 2019, **123**, 027401.
61 E. Liu, J. van Baren, T. Taniguchi, K. Watanabe, Y.-C. Chang and C. H. Lui, *Phys. Rev. Res.*, 2019, **1**, 032007.
62 M. A. McGuire, H. Dixit, V. R. Cooper and B. C. Sales, *Chem. Mater.*, 2015, **27**, 612–620.
63 B. Huang, G. Clark, E. Navarro-Moratalla, D. R. Klein, R. Cheng, K. L. Seyler, D. Zhong, E. Schmidgall, M. A. McGuire, D. H. Cobden, W. Yao, D. Xiao, P. Jarillo-Herrero and X. Xu, *Nature*, 2017, **546**, 270–273.
64 W. Chen, Z. Sun, Z. Wang, L. Gu, X. Xu, S. Wu and C. Gao, *Science*, 2019, **366**, 983–987.
65 L. Thiel, Z. Wang, M. A. Tschudin, D. Rohner, I. Gutiérrez-Lezama, N. Ubrig, M. Gibertini, E. Giannini, A. F. Morpurgo and P. Maletinsky, *Science*, 2019, **364**, 973–976.
66 T. Zhang, M. Grzeszczyk, J. Li, W. Yu, H. Xu, P. He, L. Yang, Z. Qiu, H. Lin, H. Yang, J. Zeng, T. Sun, Z. Li, J. Wu, M. Lin, K. P. Loh, C. Su, K. S. Novoselov, A. Carvalho, M. Koperski and J. Lu, *J. Am. Chem. Soc.*, 2022, **144**, 5295–5303.
67 J.-U. Lee, J. Park, Y.-W. Son and H. Cheong, *Nanoscale*, 2015, **7**, 3229–3236.
68 J. Wierzbowski, J. Klein, F. Sigger, C. Straubinger, M. Kremser, T. Taniguchi, K. Watanabe, U. Wurstbauer, A. W. Holleitner, M. Kaniber, K. Müller and J. J. Finley, *Sci. Rep.*, 2017, **7**, 12383.
69 X. Hua, T. Axenie, M. N. Goldaraz, K. Kang, E.-H. Yang, K. Watanabe, T. Taniguchi, J. Hone, B. Kim and I. P. Herman, *ACS Appl. Mater. Interfaces*, 2022, **14**, 2255–2262.
70 J. P. Perdew, K. Burke and M. Ernzerhof, *Phys. Rev. Lett.*, 1996, **77**, 3865–3868.
71 G. Kresse and J. Furthmüller, *Comput. Mater. Sci.*, 1996, **6**, 15–50.
72 G. Kresse and D. Joubert, *Phys. Rev. B: Condens. Matter Mater. Phys.*, 1999, **59**, 1758–1775.
73 P. E. Blöchl, *Phys. Rev. B: Condens. Matter Mater. Phys.*, 1994, **50**, 17953–17979.
74 S. Grimme, *J. Comput. Chem.*, 2006, **27**, 1787–1799.

 This journal is © The Royal Society of Chemistry 2025